Journal of Alloys and Compounds 1060 (2026) 187319

Contents lists available at ScienceDirect

Journal of Alloys and Compounds

journal homepage: www.elsevier.com/locate/jalcom

Tunable interface coupling in V_2O_5/SnS_2 hybrid nanocomposite for efficient ammonia monitoring at room temperature

Nguyen Pham Yen Nhi, Nguyen Cao Nam, Nguyen Van Duy *, Chu Manh Hung, Chu Thi Xuan, Dang Thi Thanh Le, Nguyen Duc Hoa *

School of Materials Science and Engineering, HaNoi University of Science and Technology, 1 Dai Co Viet Street, Bach Mai ward, Ha Noi 100000, Viet Nam

ARTICLE INFO

Keywords:
NH_3 gas sensor
V_2O_5/SnS_2 nanocomposite
Room-temperature
Interfacial engineering

ABSTRACT

Ammonia (NH_3) gas sensors are indispensable in agriculture, industry, and environmental safety; however, achieving high sensitivity at room temperature remains a challenge. In this study, we report a mechanical blended V_2O_5/SnS_2 composite synthesized via a facile hydrothermal route that delivers outstanding NH_3 detection performance at room temperature. Among various tested samples, the VS15 composite with composition V_2O_5:SnS_2 of 1:5 exhibits a remarkable response of 2.39 toward 500 ppm NH_3, which is 2.26 times higher than pristine V_2O_5—along with rapid response dynamics (149 s). The VS15 sensor also demonstrates good reusability and strong selectivity against interfering gases such as NO_2, C_2H_6O, H_2, C_3H_8O, C_3H_6O and C_2H_4. Unlike conventional heterojunction-driven systems, the sensing enhancement originates from synergistic interfacial effects, including increased surface-active sites, accelerated adsorption–desorption kinetics, and promoted redox interactions with NH_3 molecules. This work presents a cost-effective and scalable interfacial engineering strategy for binary semiconductor systems, paving the way for next-generation, low-power gas sensors with broad potential in environmental monitoring, healthcare diagnostics, and wearable electronics.

1. Introduction

In modern society, ammonia (NH_3) is a volatile inorganic gas released in substantial amounts from various anthropogenic sources, including fertilizer production, industrial refrigeration systems, intensive livestock and poultry farming [1,2]. Excessive exposure to NH_3 poses severe threats to human health, causing eye and skin irritation, respiratory distress, impaired immunity, asthma, and, at high levels, even death [1–3]. The National Institute for Occupational Safety and Health (NIOSH) recommends an exposure limit of 25 ppm as an 8-hour time-weighted average and 35 ppm as a short-term exposure limit over 15 min [4]. Beyond its direct toxicity, NH_3 contributes significantly to the formation of fine particulate matter (PM2.5), a hazardous air pollutant capable of penetrating deep into the lungs and bloodstream. This secondary pollutant increases the risk of cardiovascular diseases, cancer, and respiratory illnesses [5,6]. Concurrently, NH_3 is also attracting attention as a promising clean energy carrier. With its high hydrogen density, it enables efficient storage and long-distance transportation of hydrogen, acting as a critical link in the hydrogen supply chain and offering a sustainable alternative to fossil fuels [7–9]. Given its dual nature as both a hazardous pollutant and a potential energy vector, the development of high-performance NH_3 gas sensors is of paramount importance, requiring high sensitivity, selectivity, repeatability, long-term stability, and low power consumption at room-temperature operation.

Among the diverse materials investigated for gas sensors, semiconducting metal oxides (SMOs) such as SnO_2 [10,11], ZnO [12,13], In_2O_3 [14,15], … have long been preferred owing to their simple crystal structures, high sensitivity, and stability. Nevertheless, their practical use in mobile, wearable, or harsh-environment platforms is constrained by poor selectivity and the necessity of high operating temperatures, which lead to increased power consumption [9,16–18]. In parallel, two-dimensional (2D) materials such as graphene, SnS_2, MoS_2, and MXenes exhibit large surface-to-volume ratios, ultrathin thickness, and abundant active sites, thereby enhancing gas adsorption, charge transfer, and interfacial interactions [19,20]. While their integration into gas sensing has improved both sensitivity and selectivity, making them promising for room-temperature applications, these 2D materials still suffer from sluggish response/recovery dynamics at low temperatures and limited long-term stability [21–23].

* Corresponding authors.
E-mail addresses: duy.nguyenvan@hust.edu.vn (N. Van Duy), hoa.nguyenduc@hust.edu.vn, ndhoa@itims.edu.vn (N.D. Hoa).

https://doi.org/10.1016/j.jallcom.2026.187319
Received 22 December 2025; Received in revised form 7 March 2026; Accepted 11 March 2026
Available online 12 March 2026

To overcome these limitations, hybrid heterostructures that integrate 2D materials with SMOs to form heterojunctions have emerged as an effective approach [24]. This interfacial engineering approach not only modulates gas–solid interaction pathways but also accelerates oxygen adsorption–desorption kinetics, ultimately enhancing gas sensing performance. For instance, a MoS_2/ZnO heterostructure developed by Gond et al. exhibited an exceptional response of 100.4% to 50 ppm NH_3 at room temperature [25]. More recently, a self-powered rGO/SnO_2 nanocomposite sensor was reported to show superior selectivity, covering a broad detection range of 15–1600 ppm and delivering a 5.2% response to 800 ppm NH_3 within 22 s at room temperature [26]. Among various SMOs, V_2O_5 has emerged as a focal sensing material because the flexible oxidation states of vanadium enable tunable defect populations and govern gas–molecule chemisorption at the sensing interface. Typically, V_2O_5 nanostructures generally exhibit n-type conductivity; however, upon exposure to NH_3 at elevated temperatures, they can undergo a polarity inversion from n-type to p-type, offering valuable mechanistic insights into the sensing process [27]. The gas sensor based on bare V_2O_5 materials could detect different gases [28]. For instance, the V_2O_5 thin film was used for detection of hydrogen, methane, and propane [29], whereas the bare V_2O_5 nanorods were used for detection of NH_3 [30]. In addition, the Cu doped V_2O_5 thin film was also used for gas sensor, where it exhibited a response of 40.7% for 8880 ppm CO_2 at room temperature [31]. Despite these advances, research on V_2O_5-based heterostructures remains surprisingly limited, even though V_2O_5 offers rich surface redox chemistry and variable oxidation states that could be highly beneficial for NH_3 sensing devices. The gas sensor based on bare V_2O_5 materials suffer from limitations such as requiring high operating temperature, and having low sensitivity [32], with slow response and recovery time [30]. Note that the bare V_2O_5 spherical flower like nanostructure exhibited a response of about 1.06 towards 500 ppm at room temperature [32].

Additionally, tin disulfide (SnS_2) has also emerged as a particularly promising n-type 2D semiconductor. Its relatively wide band gap (~2.0–2.4 eV) and favorable electronegativity provide an excellent foundation for next-generation NH_3 sensing platforms, especially when integrated into hybrid heterostructures [33,34]. The SnS_2 materials and their composites of different morphologies were used for gas sensors to detect different gases such as NO_2 [35,36]; triethylamine [37],and NH_3 [38]. The bare SnS_2 microflowers exhibited a response low of about 80% toward 100 ppm NH_3 at room temperature [39]. However, composites of SnS_2 with other materials were reported to enhance the gas sensing performance [40]. For example, the Pr-SnS_2/ZnS exhibited a response of about 160 towards 2000 ppm NH_3 at 160 °C [38], whereas the SnS_2 nanosheets decorated with $Ti_3C_2T_x$ exhibited a response of 86.35% towards 500 ppm NH_3 at room temperature [41]. Therefore, the combination of 2D materials of V_2O_5 and SnS_2 is well worth waiting for enhancement of gas sensing performance via utilizing the synergic effect of p–n heterojunction, large surface area of 2D materials, and improved charge transport at the interface [42]. However, systematically investigation on the preparation, and enhancement of gas sensing characteristics of V_2O_5 nanorods and 2D SnS_2 nanosheets have not been fully studied yet.

Here, we report the rational design of a V_2O_5/SnS_2 nanocomposite synthesized via a facile hydrothermal route. The optimized composite achieves a 2.26-fold higher response than pristine V_2O_5 toward 500 ppm NH_3, along with fast response/recovery dynamics at room temperature. This enhancement is attributed not only to the increased density of surface-active sites but also to accelerated interfacial charge transfer and redox interactions at the V_2O_5/SnS_2 heterojunction. Beyond demonstrating high-performance room-temperature sensing, our findings highlight interfacial engineering of binary semiconductors as a versatile and scalable strategy to tailor gas–solid interactions, paving the way toward next-generation, energy-efficient, and portable gas sensing technologies.

2. Experimental

2.1. Chemicals

Ammonium metavanadate (NH_4VO_3), tin (IV) chloride pentahydrate ($SnCl_4{\cdot}5H_2O$), thiourea (CH_4N_2S), oxalic acid ($H_2C_2O_4{\cdot}2H_2O$), hydrochloric acid (HCl), ethylene glycol, Pluronic P123 (surfactant), ethanol, acetone, and N-vinylpyrrolidone (NVP) were used as purchased without purification. All reagents were of analytical grade and were used as received without further purification.

2.2. Preparation of SnS_2/V_2O_5 nanocomposites

2.2.1. Synthesis of pristine V_2O_5

V_2O_5 nanorods were synthesized via a hydrothermal method, as illustrated in Fig. 1a. In a typical procedure, 10 mmol NH_4VO_3 was vigorously stirred in a mixed solvent of 30 mL ethylene glycol and 30 mL deionized water for 15 min. Subsequently, 1 g of Pluronic P123 and 10 mmol of oxalic acid were added sequentially under continuous stirring. The resulting solution was transferred into a 100 mL Teflon-lined stainless-steel autoclave and maintained at 200°C for 24 h. The obtained precipitate was washed several times with deionized water and ethanol, followed by drying at 80°C for 24 h in air [27].

2.2.2. Synthesis of pristine SnS_2

SnS_2 nanosheets were prepared using a similar hydrothermal approach (Fig. 1b). Briefly, 2 mmol $SnCl_4{\cdot}5H_2O$ was dispersed in a solution containing hydrochloric acid (HCl), 16 mmol thiourea, and 60 mL deionized water. The mixture was stirred for 30 min and then transferred into a 100 mL Teflon-lined stainless-steel autoclave, followed by hydrothermal treatment at 200°C for 24 h. The resulting precipitate was collected, washed repeatedly with deionized water and ethanol, and dried at 80°C for 24 h, using the same procedure as for V_2O_5 [43].

2.2.3. Preparation of V_2O_5/SnS_2 nanocomposites

The as-prepared SnS_2 and V_2O_5 powders were ground using an agate mortar for about 15 min to obtain fine particles, and then mechanically blended at different mass ratios V_2O_5:SnS_2 of 10:1, 5:1, 1:1, 1:5, and 1:10, denoted as VS101, VS51, VS11, VS15, and VS110, respectively.

2.2.4. Fabrication of gas sensor devices

Gas sensor devices were fabricated on Pt interdigitated electrodes (IDEs) patterned on SiO_2 substrates through standard microfabrication processes. Each electrode finger had a width of 20 μm and an inter-finger spacing of 20 μm [10]. Prior to material deposition, the substrates were sequentially cleaned with acetone, ethanol, and deionized water, followed by drying at 100 °C in air. The as-prepared V_2O_5/SnS_2 nanocomposite was dispersed in N-vinylpyrrolidone (NVP) and ultrasonicated for 30 min to obtain a homogeneous suspension. The resulting dispersion was drop-cast onto the pre-cleaned IDEs. Finally, the devices were subjected to vacuum annealing at 300 °C under an argon (Ar) atmosphere, as illustrated in Fig. 2.

2.2.4.1. Gas sensing measurements. The gas sensing performance was evaluated using a customized measurement system equipped with mass flow controllers (MFCs) to precisely regulate and blend standard gases with ambient air, thereby generating target analyte concentrations. All measurements were carried out under a constant bias voltage of ±5 V. Further details about the gas sensing measurement system were reported elsewhere [10]. The sensor response (S) was defined as:

$$S = \frac{R_g}{R_a}$$

where R_g and R_a represent the sensor resistance in the presence of the target gas and in air, respectively. The response time and recovery time

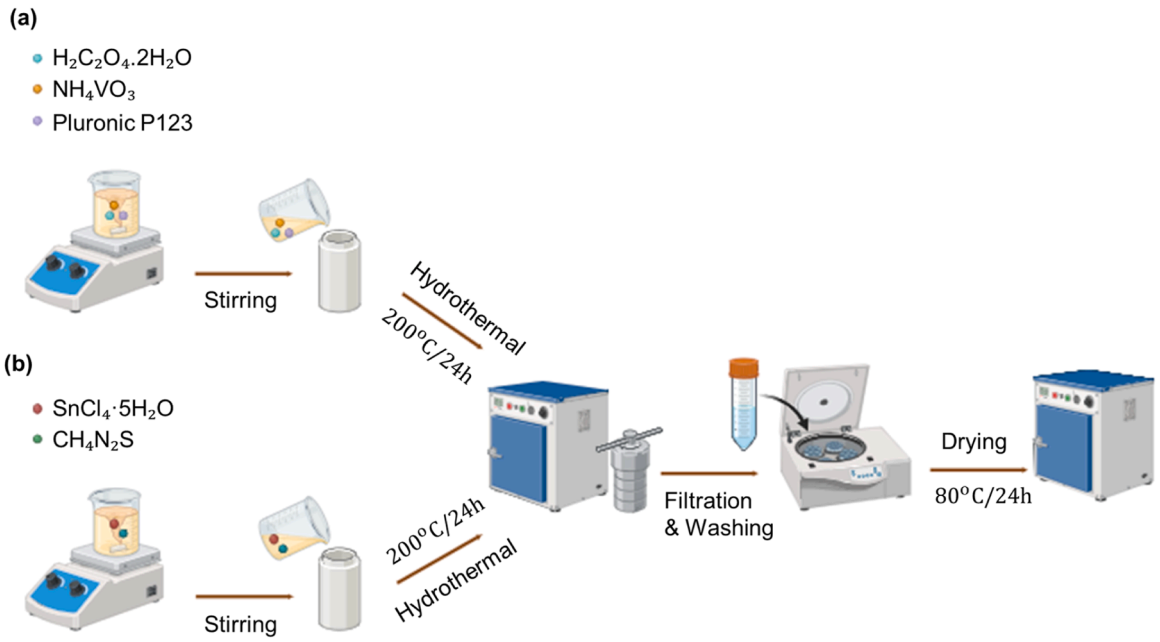

Fig. 1. Schematic illustration of material synthesis (a) V_2O_5 and (b) SnS_2 prepared via the hydrothermal method.

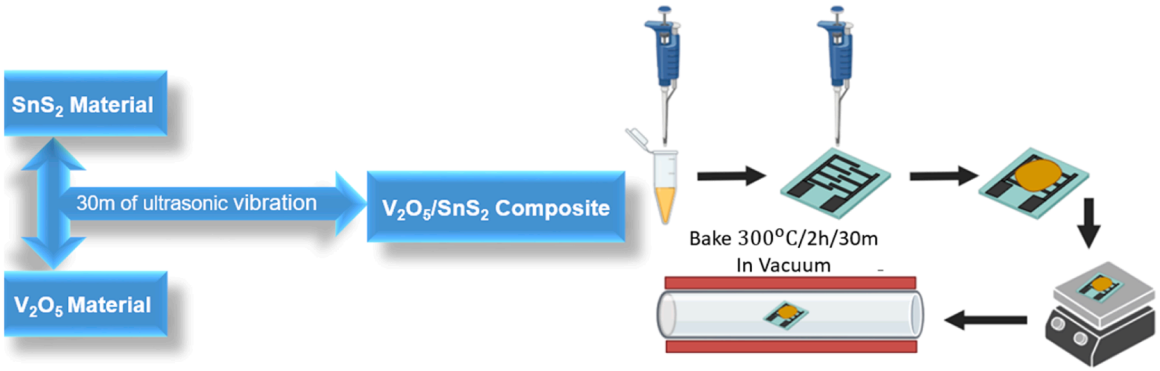

V_2O_5/SnS_2 Mass Ratio	10/1	5/1	1/1	1/5	1/10
Sample	VS101	VS51	VS11	VS15	VS110

Fig. 2. Schematic illustration of the fabrication process of V_2O_5/SnS_2 nanocomposite-based gas sensors with different mass ratios.

were defined as the time required for the sensor resistance to reach 90% of the total change upon exposure to and removal of the target gas, respectively.

3. Results and discussion

3.1. Material characterization

X-ray diffraction (XRD) analysis was performed on a D2 Phaser - 2nd Gen - Bruker diffractometer (Germany) to determine the crystalline structures of the as-prepared materials. Fig. 3 displays the XRD patterns of pristine V_2O_5 and SnS_2 nanomaterials. For the V_2O_5, distinct diffraction peaks appeared at 15.3°, 20.3°, 21.7°, 26.1°, 31.0°, 32.4°, 34.3°, 41.3°, 45.5°, 48.8°, 51.2°, 52.0°, 55.6°, 61.1°, and 62.1°, which are indexed to the (200), (001), (101), (110), (301), (011), (310), (002), (411), (012), (020), (601), (021), (321), and (710) crystal planes, respectively. These results confirm the successful formation of orthorhombic V_2O_5 phase, in excellent agreement with JCPDS No. 41–1426 [44]. For pristine SnS_2, sharp peaks were observed at 14.8°, 28.9°, 30.2°, 32.0°, 41.7°, 46.0°, 49.8°, 52.4°, 54.9°, 58.4°, 60.6°, 62.9°, 67.1°, and 70.3°, corresponding to the (001), (100), (002), (101), (102), (003), (110), (111), (103), (200), (201), (004), (202), and (113) planes, consistent with the hexagonal SnS_2 structure (JCPDS No. 23–0677) [43]. Upon the formation of V_2O_5/SnS_2 nanocomposites, the characteristic diffraction peaks of both constituents remained visible. The systematic variation in relative peak intensities with the mixing ratio confirms the successful integration and coexistence of both phases without significant structural degradation (Figure S1, Supplementary).

The surface morphologies of pristine V_2O_5, SnS_2 nanomaterials, and their composites were investigated by scanning electron microscopy (SEM, JEOL-3000FC, Japan). As shown in Fig. 4a, V_2O_5 is composed of short, uniformly distributed nanorods randomly orientated to form a porous network structure. Those nanorods typically exhibit an average diameter of about 100 nm, with the length of approximately 5 μm. This is a self-assembled material with highly specific morphology. To control the structure directionally, ethylene glycol acts as a key agent in the polyol process, which controls the unidirectional growth of the crystal lattice [45,46]. According to Xia et al., V_2O_5 nanorods are formed

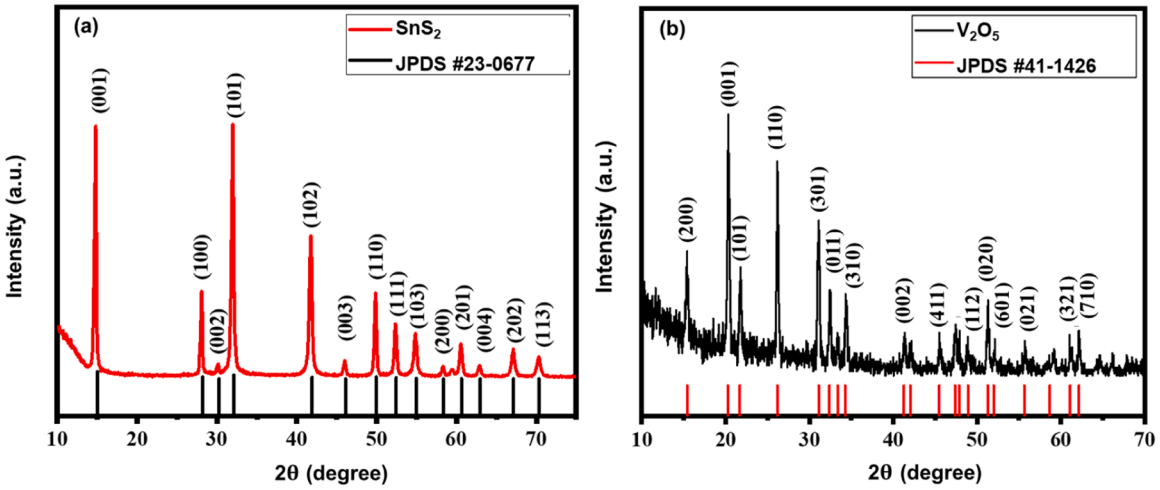

Fig. 3. XRD patterns of the (a) pristine SnS_2 and (b) pristine V_2O_5.

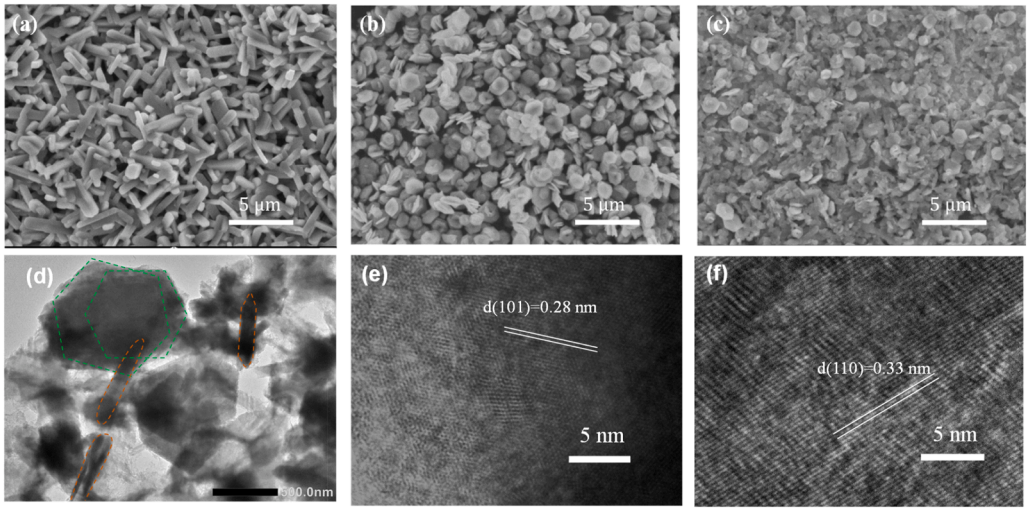

Fig. 4. SEM images of a) V_2O_5 nanorods, b) SnS_2 nanosheets, and c) VS15 composite; d, e) and f) High resolution TEM images of VS15 composite.

through two-steps mechanism: (i) coordination of ethylene glycol with vanadium ions to form vanadium glycolate precursors, and (ii) subsequent oligomerization that drives the longitudinal extension of the nanorod framework [45]. In addition, the presence of Pluronic P123 plays an important surfactant in controlling morphology. Pluronic P123, with its strong self-assembly ability, provides micelles framework that guides the nanorod growth in this study. Thus, the simultaneous interaction of these factors creates an optimal environment for the formation of uniform V_2O_5 nanorods with superior morphological control [44]. Such an interconnected structure is advantageous for facilitating gas diffusion throughout the sensing layer [47,48]. In contrast, the SnS_2 sample exhibits a well-defined 2D hexagonal flake-like architecture, consisting of hierarchically stacked ultrathin nanosheets with thicknesses of several tens of nanometers, stacked in a relatively uniform manner (Fig. 4b). The hexagonal SnS_2 layered nanosheets are formed via a heterogeneous nucleation mechanism without any additives. SnS_2 exhibits a CdI_2-type layered structure, in which the Sn atoms are sandwiched between two hexagonally packed S layers; these layers stack along the c-axis, facilitating 2D-oriented growth. From the primary crystalline grains, phase transformation and directional morphological evolution, governed by an Ostwald ripening process and heterogeneous nucleation, lead to the formation of sharp, uniform hexagonal nanosheets. Careful control of temperature, reaction time, and precursor chemistry determines the structural uniformity and completeness of the resulting 2D nanosheets, as reported in our previous study [43,49]. This morphology provides a large accessible surface area, enhancing gas adsorption and the interaction with analyte molecules [50]. Upon hybridization, the V_2O_5/SnS_2 composites displayed distinct morphologies depending on the mixing ratio (Figure S2, Supplementary). Notably, the VS15 sample reveals a highly porous and homogeneously distributed nanostructure, where V_2O_5 nanorods are intimately interwoven with SnS_2 nanosheets (Fig. 4c). During mechanical grinding, the two materials undergo distinct fracture mechanisms dictated by their intrinsic structural characteristics. For SnS_2, the CdI_2-type layered framework is highly susceptible to exfoliation, which disrupts the long-range stacking order. In contrast, the self-assembled V_2O_5 nanorods possess relatively weak inter-rod and intra-rod bonding; consequently, under mechanical stress, they are readily cleaved along their preferential growth direction, yielding shorter and thinner rod-like fragments. Thus, the milling process simultaneously partially destroys the layered architecture of SnS_2 and fragments the V_2O_5 nanorods into smaller structural domains. Although the original morphologies of SnS_2 and V_2O_5 are partially degraded, such mechanical fragmentation can be beneficial for gas-sensing performance. First, the reduction in particle size increases the density of accessible active sites available for NH_3 adsorption. Second, the interwoven composite architecture facilitates the formation of

abundant V_2O_5-SnS_2 heterointerfaces, which promote charge transfer and modulate the electronic structure of the sensing layer. Consequently, this integrated network constructs a more interconnected and catalytically active framework, laying the structural foundation for the superior NH_3 sensing characteristics discussed in the following sections.

Transmission electron microscopy (TEM) images (Fig. 4e-f) reveal nanoscale domains of both constituents, where the SnS_2 nanosheets preserve their characteristic layered architecture. In contrast, the V_2O_5 nanorod regions appear as compact, irregular fragments, resulting fracture-mediated downsizing during the milling process. This heterogeneous distribution further underscores the successful integration of the two phases and fully corroborates the SEM observations. Despite localized densification, the structural signatures of each component remain clearly discernible, confirming the composite nature of the V_2O_5/SnS_2 heterostructure. The morphology of the SnS_2 nanosheets and V_2O_5 nanorods retained after composite preparation, indicating that the grinding process did not damage the structure of the materials. High resolution TEM images of SnS_2 and V_2O_5 shown in Figs. 4(g), and 4(h), respectively. Both samples reveal high crystallinity with clear lattice fringes indicating a relatively high crystallinity of V_2O_5 and SnS_2. The interplanar spacing in Fig. 4(g) is estimated to be approximately 0.28 nm, which matches well with the (101) plane of hexagonal SnS_2 documenting the preferential growth orientation along the (101) plane [51]. High resolution TEM image of V_2O_5 displays and continuous lattice fringes suggest well-developed crystals with minimal structural defects in the observed region. In addition, the interplanar spacing is estimated to be approximately 0.34 nm (Fig. 4h), corresponding to the (110) plane of orthorhombic α-V_2O_5 [52].

To further elucidate the composition of the VS15 sample, energy-dispersive X-ray spectroscopy (EDX) analysis was conducted. The spectrum unequivocally confirms the presence of Sn, S, V, and O, consistent with V_2O_5/SnS_2 heterostructure and indicating high material purity (Fig. 5). Based on the 1:5 mass ratio of V_2O_5 to SnS_2 used for VS15, the theoretical weight percentages should be approximately 9.3 wt% for V, 54.1 wt% for Sn, and 29.2 wt% for S. However, the measured values of 27.81 wt% for V and 31.32 wt% for Sn are much closer than expected, indicating a deviation from the ideal bulk stoichiometry.

This discrepancy primarily originates from the surface-sensitive nature of EDX and the markedly different fracture behaviors of SnS_2 and V_2O_5 during mechanical milling because V_2O_5 nanorods are prone to longitudinal fragmentation and easily squeeze into empty space on the surface of the composite. This is accompanied by the relatively low sulfur content (16.37 wt%, 17.90 at%) and the strong oxygen signal (24.50 wt%, 53.71 at%) further confirming the prevalence of vanadium oxide domains within the probed region. Therefore, the EDX data reflects the surface-enriched oxide domains rather than the true bulk stoichiometry. Such an oxide-rich surface environment is expected to influence the electronic structure strongly, promote oxygen chemisorption and enhance interfacial redox interaction with NH_3 molecules, thereby underpinning the superior sensing performance observed in VS15 [53].

Raman speatra was also for further characterization of the composite. As depicted in Fig. 5(b), the Raman spectra of the V_2O_5/SnS_2 composite displays dominant peaks at 136, 277, 402, 688, and 986 cm^{-1} of orthorhombic V_2O_5 [27]. The red shift in Raman mode of V_2O_5 is possible due to the presence of SnS_2, which induces the charge transfer and electronic interaction at the heterojunction interface of composite. A distinct peak appears at 309 cm^{-1} can be attributed to the overlapping of the V-O bending mode of V_2O_5 (304 cm^{-1}) and the out-of-plane A_{1g} stretching mode of SnS_2 (314 cm^{-1}) [50]. The shift of the A_{1g} mode from its typical 314 cm^{-1} position to 309 cm^{-1} reflects the mechanical tensile strain caused by the formation of V_2O_5/SnS_2 composite.

3.2. Gas Sensing Properties

The gas sensing performance of the V_2O_5/SnS_2 nanocomposites was systematically evaluated at room temperature (Fig. 6). The dynamic response-recovery curves of different composite ratios (Fig. 6**a**) exhibit a sharp increase in resistance upon exposure to NH_3, followed by a slower and incomplete recovery upon gas removal. This overall response pattern is characteristic of the interaction between a reducing gas (NH_3) and a p-type semiconductor. Among all samples, the VS15 composite exhibited the highest response, significantly outperforming the other ratios.

To further assess the sensing performance, a calibration curve was plotted (Fig. 6b), showing a clear linear correlation between response and NH_3 concentration across 10–500 ppm range. Notably, the VS15 sensor displayed the steepest and the strongest sensitivity, with response values of 1.16, 1.27, 1.36, 1.50, 1.79, and 2.39 at 10, 20, 40, 100, 250, and 500 ppm NH_3, respectively. At 500 ppm, VS15 exhibited the highest response of 2.39, clearly surpassing VS110 (1.79), VS51 (1.60), VS11 (1.45), and VS101 (1.30). This response is approximately 2.26 folds greater than that of pristine V_2O_5 (1.06). The enhanced performance is attributed to the synergistic integration of the large specific surface area of 2D SnS_2 nanosheets and the strong oxidizing capability of V_2O_5 nanorods. This combination optimizes charge transfer efficiency and facilitates favorable adsorption–reduction interactions with NH_3 molecules. Consequently, the composition ratio is a decisive factor in tuning sensing properties, with the 1:5 ratio (VS15) emerging as the optimal configuration. Based on these results, the VS15 sensor was selected for further studies, including response/recovery dynamics, selectivity, and

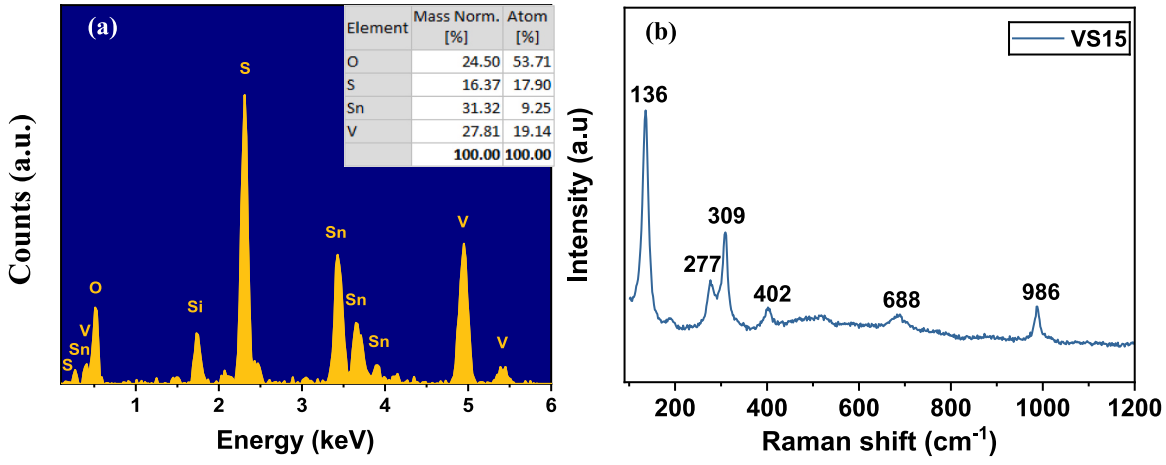

Fig. 5. (a) EDX spectrum of the VS15 composite; and (b) Raman spectra of the SV15 composite.

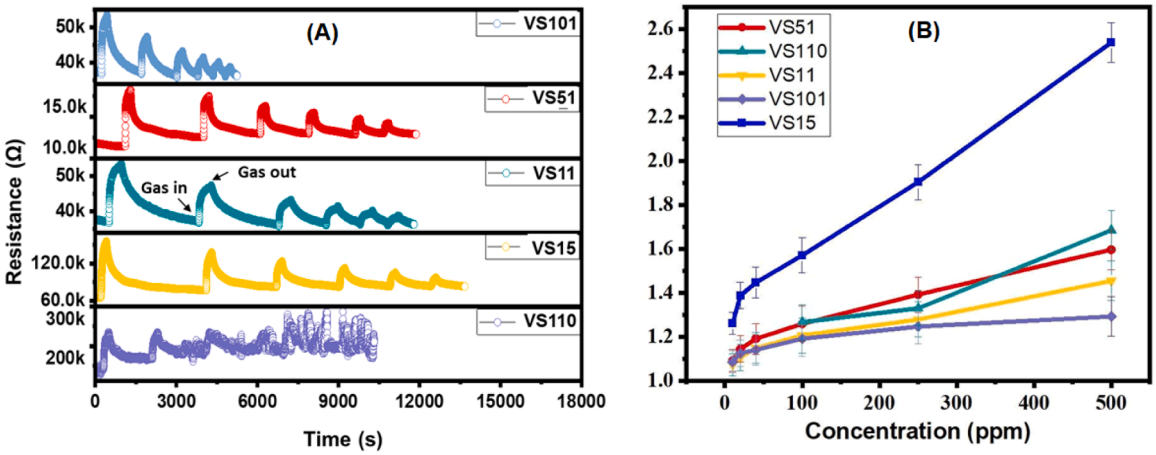

Fig. 6. Comparative gas sensing performance of V_2O_5/SnS_2 sensors with different composition ratios. (a) Real-time resistance responses of VS101, VS51, VS11, VS15, and VS110 sensors toward various concentrations of NH_3 at room temperature. (b) Calibration plots of response versus NH_3 concentration.

repeatability.

The selectivity of the V_2O_5/SnS_2-based sensor was tested for the detection of 500 ppm of NO_2, C_2H_6O, H_2, NH_3, C_3H_8O, C_3H_6O and C_2H_4 at room temperature (Fig. 7). The sensor exhibited a robust and rapid response specifically toward NH_3 ($R = 2.39$, $\tau_{(res)} = 149$ s). In contrast, the responses to other interfering gases, such as NO_2 (1.0), C_2H_6O (1.0), H_2 (1.25), C_3H_8O (1.0), C_3H_6O (1.0), and C_2H_4 (1.22) were relatively negligible (Fig. 7a, b). These results demonstrate the highest selectivity of the device toward NH_3, which can be ascribed to the strong affinity between electron-rich NH_3 molecules and the surface-active sites associated with high-valence vanadium in the V_2O_5 phase. In addition, the favorable heterointerface between V_2O_5 and SnS_2 facilitates efficient charge transfer, further amplifying the sensing response.

The repeatability of the VS15 sensor was further examined by subjecting it to six consecutive exposure/recovery cycles with 10 ppm NH_3 at room temperature (Fig. 7d). Over the six cycles, the sensor maintained nearly identical response amplitudes with a relative standard deviation (RSD) as low as 0.97%, confirming its high repeatability. Although the sensor maintained a reproducible response pattern, a slight baseline drift and minor fluctuations in signal intensity were observed across the cycles. This behavior is not unique to our system but has also been widely reported in many NH_3 sensors due to the strong binding energy

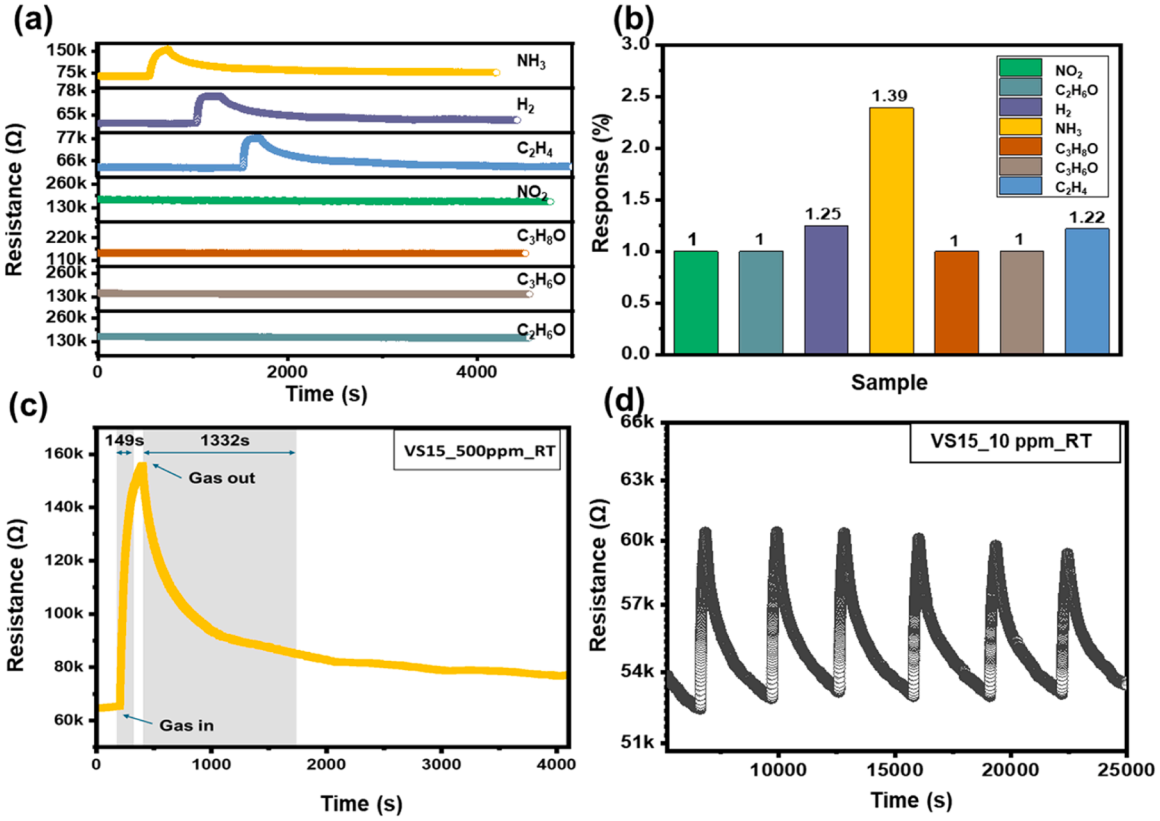

Fig. 7. Gas sensing characteristics of the VS15 sensor at room temperature. (a) Real-time resistance responses toward 500 ppm of different target gases (NO_2, C_2H_6O, H_2, NH_3, C_3H_8O, C_3H_6O and C_2H_4). (b) Comparison of response values, highlighting the high selectivity toward NH_3. (c) Dynamic response–recovery curve of the sensor to 500 ppm NH_3. (d) Repeatability of the sensor over six consecutive exposure/recovery cycles to 10 ppm NH_3.

between NH_3 molecules and active sites, which often impedes complete desorption [54–56]. Further optimization of recovery conditions (e.g., UV illumination or mild thermal activation) and tailoring of surface defect chemistry may therefore be required to achieve improved repeatability in future studies [55,57–59].

Nevertheless, the synergistic interplay between V_2O_5 redox activity and SnS_2 interfacial charge modulation yields a remarkable response at room temperature, underscoring the potential of this composite design for practical low-power NH_3 detection. However, the effect of humidity and long-term stability of the sensor should be studied under different working conditions for practical application. This is carried out in our lab, and the results will be reported elsewhere.

For comparison with previously reported sensors, Table 1 summarizes several recent studies on V_2O_5-based gas sensors, providing a benchmark for evaluating the performance of the hydrothermally synthesized V_2O_5/SnS_2 composite developed in this work. In particular, the VS15 sensor demonstrates a highly competitive response at room temperature, outperforming or matching many state-of-the-art V_2O_5-based systems. This superior performance highlights the effectiveness of our composite strategy in synergistically integrating 2D SnS_2 nanosheets with V_2O_5 nanorods. These findings underscore the significant promise of this material platform as a robust candidate for practical, low-power NH_3 detection.

3.3. Gas sensing mechanism

The gas sensing mechanism in composite materials is typically more intricate than that of their single-phase counterparts. The enhanced NH_3 sensing performance of the V_2O_5/SnS_2 composite, compared to pristine V_2O_5, is not only governed by conventional adsorption–desorption reactions but is also strongly boosted by synergistic effects arising from the unique surface architecture and interfacial heterojunctions. Specifically, the interfacial region between V_2O_5 and SnS_2 facilitates directional charge transfer and modulates the electronic structure, thereby strengthening surface reactions with analyte molecules. In this composite, V_2O_5 (p-type) – a prototypical semiconducting metal oxide with a high oxidation state of vanadium (V^{5+}) – acts as an active redox center, whereas the 2D SnS_2 nanosheets provide efficient gas diffusion pathways and a high surface-to-volume ratio. At room temperature, the activation energy required for surface reactions is generally difficult to overcome [68]. Thus, the expanded surface-to-volume ratio and abundant interfacial sites become crucial factors that lower the reaction barrier, promote charge carrier exchange, and accelerate the overall sensing kinetics.

The sensing mechanism is illustrated in Fig. 8, and the reaction process can be described through the following Eqs. (1–5) [69,70]. In air, oxygen molecules are adsorbed on the surface of V_2O_5 by extracting electrons from the valence band of the p-type-dominated composite, forming reactive chemisorbed oxygen species (O_2^-, O^-). This surface redox process increases the hole accumulation layer (HAL) near the surface, resulting in a relatively low baseline resistance. Upon exposure to NH_3 (a strong reducing gas), NH_3 molecules react with the chemisorbed oxygen species and donate electrons that recombine with majority hole carriers, leading to a reduction in hole concentration in p-type V_2O_5 and HAL region. Consequently, the band bending is enhanced and the overall resistance increases (Rg > Ra), which is characteristic of p-type sensing behavior.

Together with the reaction on the surface of p-type V_2O_5, the formation of the depletion region occurred at the interface of V_2O_5/SnS_2 due to the charge diffusion from n-type SnS_2 to p-type V_2O_5. However, due to the dominant p-type nature in composite sample, electrical conduction is mainly governed by the hole transport network, thus the sensor exhibits the p-type semiconducting characteristics. The adsorption of NH_3 molecules lead to modulation occurring both at the material surface and across the V_2O_5/SnS_2 heterointerface, yielding a synergistically amplified response compared to single-phase systems. However, an observable phenomenon is that the sensor's current signal does not fully return to the baseline after NH_3 desorption, displaying a slight baseline drift. This can be explained by the fact that NH_3 molecules are preferentially adsorbed at defect sites, vacancies, and edge folds on the SnS_2 nanosheets, where the adsorption energy is relatively high. These sites hinder complete desorption and trap charge carriers, thereby slowing recovery kinetics [2]. This behavior is commonly reported in state-of-the-art NH_3 sensors, underscoring that optimization of recovery strategies (e.g., UV-assisted desorption, mild thermal activation, or surface defect engineering) remains critical for practical applications [71]. Nevertheless, the synergistic interplay between V_2O_5 p-type redox activity and SnS_2 interfacial charge modulation yields a remarkable response at room temperature, underscoring the potential of this composite design for practical low-power NH_3 detection.

Oxygen adsorption in air [72,73]:

$$O_2\ (g) \rightarrow O_2\ (abs) \quad (1)$$

$$O_2\ (abs) + e^- \rightarrow O_2^-\ (abs) \quad (2)$$

$$O_2^-\ (abs) + e^- \rightarrow 2O^-\ (abs) \quad (3)$$

$$O^-\ (abs) + e^- \rightarrow O^{2-}\ (abs) \quad (4)$$

Reaction with NH_3 (reducing gas) [74]:

$$NH_3(abs) + O_x^{n-}(abs) \rightarrow N_2 + H_2O + ne^- \quad (5)$$

$$e^- + h^\circ = Null \quad (6)$$

As reported by density functional theory (DFT) calculations, the adsorption energy of NH_3 on the surface of V_2O_5 (-1.33 eV) [75] is higher than that on the surface of SnS_2 (-0.15 eV) [76]. Thus, upon exposure of the V_2O_5/SnS_2 composite to the target gas, the NH_3 molecules preferentially adsorb on the surface of V_2O_5 rather than on SnS_2. The electrons released from NH_3 upon adsorption on V_2O_5 neutralize holes and reduce the hole concentration in p-type V_2O_5. Consequently, NH_3 adsorption modulates the potential barrier at the p–n heterojunction of V_2O_5/SnS_2, leading to an increase in the overall resistance of the sensor. As a result, the sensitivity of the V_2O_5/SnS_2 composite sensor increases significantly compared to that of the individual materials.

Table 1
Comparison of NH_3 Gas Sensors Utilizing Various V_2O_5-Based Materials.

Material	Method	Operating Temperature (°C)	Concentration	Response	Reference
V_2O_5/MWCNTs	Sol-Gel	200 °C	100 ppm	20%	[60]
V_2O_5 nanosheets	Hydrothermal	RT	100 ppm	24.2%	[61]
V_2O_5 nanofibers	Wet Deposition	RT	10 ppm	1.8%	[62]
PPy/V_2O_5	Chemical Oxidation Polymerization	RT	10 ppm	19.5%	[63]
Pt NP/V_2O_5	Sputter RF Thermal Evaporation	300 °C	1000 ppm	83.2%	[64]
1%Ru@V_2O_5	Hydrothermal	RT	130 ppm	4%	[65]
V_2O_5-WO_3-TiO_2	Impregnation	550 °C	320 ppm	Not mention	[66]
V_2O_5@TiO_2	Sol-Gel	365 °C	200 ppm	8.6	[67]
V_2O_5/SnS_2	Hydrothermal	RT	500 ppm	2.39	This Work

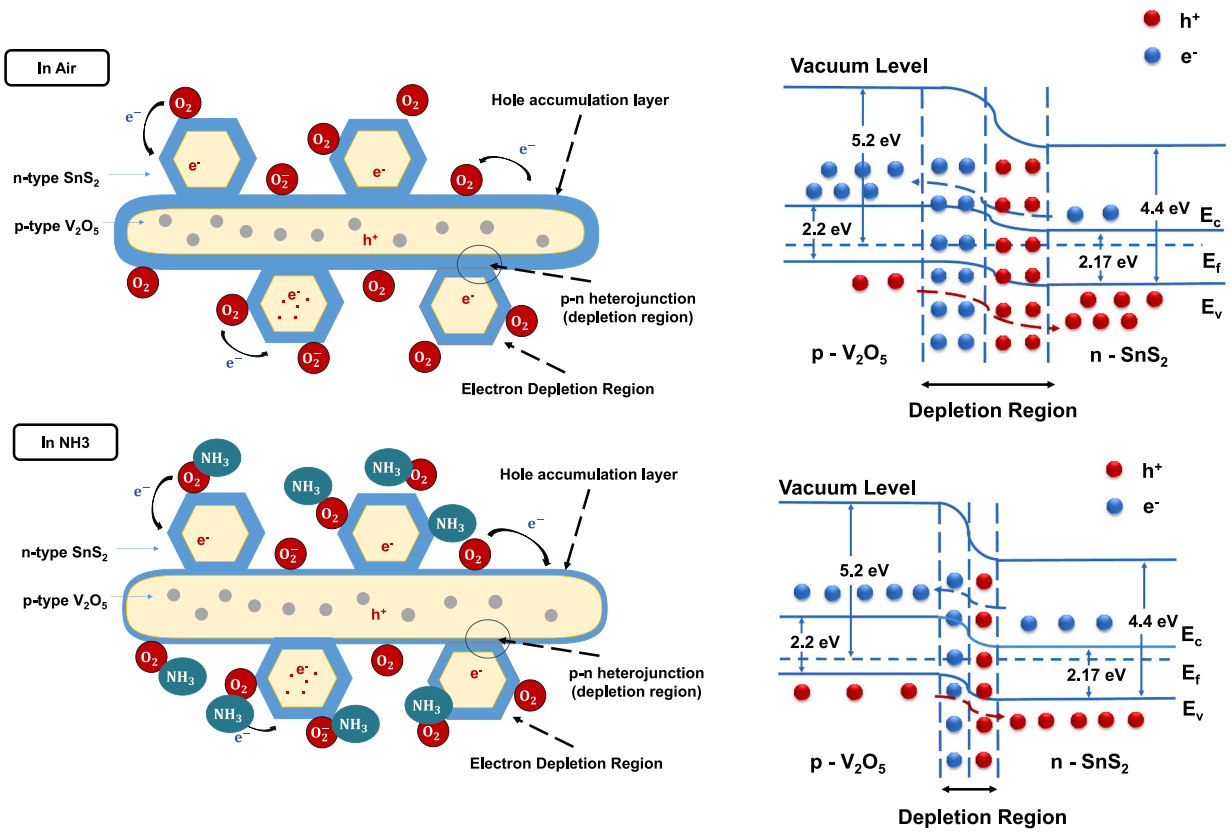

Fig. 8. Gas sensing mechanism of V_2O_5/SnS_2 in air and in the presence of NH_3 gas.

4. Conclusion

In this study, an NH_3 gas sensor based on a V_2O_5/SnS_2 composite was successfully fabricated using a simple and scalable hydrothermal synthesis combined with mechanical mixing, offering a cost-effective route for device production. The optimized VS15 sample exhibited a remarkable response of 2.39 toward 500 ppm NH_3, which is approximately 2.26 times higher than that of the pristine V_2O_5-based sensor. Moreover, the VS15 sensor exhibits superior performance, including high response, rapid reaction kinetics, and good selectivity at room temperature, highlighting the effectiveness of the composite strategy. The enhanced sensing capability can be attributed to the synergistic effects between V_2O_5 and SnS_2, which provide a large surface area, facilitate efficient charge transport, enhance surface modulation, and offer abundant active sites for NH_3 adsorption and redox reaction. These findings not only underscore the promise of V_2O_5/SnS_2 as a next-generation sensing material for room-temperature NH_3 detection but also open opportunities for integrating this composite into portable, low-power, and wearable sensing platforms. Future efforts focusing on interface engineering, defect modulation, and light-assisted recovery strategies may further boost stability and reproducibility, paving the way for real-world deployment.

CRediT authorship contribution statement

Nguyen Cao Nam: Methodology, Investigation, Formal analysis, Conceptualization. **Nguyen Van Duy:** Writing – review & editing, Supervision, Resources, Funding acquisition, Formal analysis, Conceptualization. **Nguyen Pham Yen Nhi:** Writing – original draft, Investigation, Formal analysis, Data curation. **Nguyen Duc Hoa:** Writing – review & editing, Supervision, Resources, Project administration, Conceptualization. **Chu Thi Xuan:** Visualization, Supervision, Resources, Investigation. **Dang Thi Thanh Le:** Supervision, Methodology, Investigation. **Chu Manh Hung:** Writing – review & editing, Visualization, Methodology, Investigation.

Declaration of Competing Interest

The authors declare that they have no known competing financial interests or personal relationships that could have appeared to influence the work reported in this paper.

Acknowledgment

This research is funded by Hanoi University of Science and Technology (HUST) under project number T2024-TĐ-008.

Appendix A. Supporting information

Supplementary data associated with this article can be found in the online version at doi:10.1016/j.jallcom.2026.187319.

References

[1] D. Redolfi-Bristol, et al., Ammonia toxicity and associated protein oxidation: a single-cell surface enhanced raman spectroscopy study, Chem. Res. Toxicol. 37 (1) (2024) 117–125, https://doi.org/10.1021/acs.chemrestox.3c00368.
[2] J. Bai, et al., Room-Temperature NH_3 sensor based on SnO_2 quantum dots functionalized SnS2 nanosheets, Adv. Mater. Technol. 8 (8) (2023) 1–10, https://doi.org/10.1002/admt.202201671.
[3] Z. Zhao, et al., From discovery to optimization: data-driven development of NH_3 sensing materials validated by experiments and DFT, J. Hazard. Mater. 495 (May) (2025) 139169, https://doi.org/10.1016/j.jhazmat.2025.139169.
[4] C. Yang, H. Zhang, H. Zhang, Preparation and mechanism study of highly sensitive NH_3 gas sensor based on Au-modified CdS nanoparticles, Appl. Surf. Sci. 680 (May 2024) (2025) 161389, https://doi.org/10.1016/j.apsusc.2024.161389.
[5] Y. Wu, et al., PM2.5 pollution is substantially affected by ammonia emissions in China, Environ. Pollut. 218 (x) (2016) 86–94, https://doi.org/10.1016/j.envpol.2016.08.027.

[6] K.E. Wyer, D.B. Kelleghan, V. Blanes-Vidal, G. Schauberger, T.P. Curran, Ammonia emissions from agriculture and their contribution to fine particulate matter: A review of implications for human health, J. Environ. Manag. 323 (June 2021) (2022) 116285, https://doi.org/10.1016/j.jenvman.2022.116285.

[7] S. Chatterjee, R.K. Parsapur, K.W. Huang, Limitations of Ammonia as a Hydrogen Energy Carrier for the Transportation Sector, ACS Energy Lett. 6 (12) (2021) 4390–4394, https://doi.org/10.1021/acsenergylett.1c02189.

[8] F. Alasali, M.I. Abuashour, W. Hammad, D. Almomani, A.M. Obeidat, W. Holderbaum, A review of hydrogen production and storage materials for efficient integrated hydrogen energy systems, Energy Sci. Eng. 12 (5) (2024) 1934–1968, https://doi.org/10.1002/ese3.1723.

[9] P.M. Bulemo, et al., Selectivity in chemiresistive gas sensors: strategies and challenges, Chem. Rev. 125 (8) (2025) 4111–4183, https://doi.org/10.1021/acs.chemrev.4c00592.

[10] L.V. Thong, et al., On-chip fabrication of SnO_2-nanowire gas sensor: The effect of growth time on sensor performance, Sens. Actuators B Chem. 146 (1) (2010) 361–367, https://doi.org/10.1016/j.snb.2010.02.054.

[11] M. Shahabuddin, A. Sharma, J. Kumar, M. Tomar, A. Umar, V. Gupta, Metal clusters activated SnO_2 thin film for low level detection of NH_3 gas, Sens. Actuators B Chem. 194 (2014) 410–418, https://doi.org/10.1016/j.snb.2013.12.097.

[12] B. Aydas, A. Atılgan, A. Ajjaq, S. Acar, M.F. Öktem, A. Yildiz, Flexible NH_3 gas sensors based on ZnO nanostructures deposited on kevlar substrates via hydrothermal method, Ceram. Int. 50 (18) (2024) 32477–32489, https://doi.org/10.1016/j.ceramint.2024.06.056.

[13] R.S. Ganesh, et al., Tuning the selectivity of NH_3 gas sensing response using Cu-doped ZnO nanostructures, Sens. Actuators A Phys. 269 (2018) 331–341, https://doi.org/10.1016/j.sna.2017.11.042.

[14] L. Gao, J. Xu, X. Yang, C. Xu, X. Wang, Q. Jin, Waveguide microwave gas sensor based on monolithic In_2O_3 for enhanced ammonia detection, Talanta 293 (January) (2025) 128122, https://doi.org/10.1016/j.talanta.2025.128122.

[15] I.L.P. Raj, et al., High sensitive room temperature NH_3 gas sensing properties of Bi-doped In2O3 thin films coated by nebulizer spray pyrolysis method, Surf. Interfaces 58 (August 2024) (2025) 105769, https://doi.org/10.1016/j.surfin.2025.105769.

[16] K.G. Krishna, S. Parne, N. Pothukanuri, V. Kathirvelu, S. Gandi, D. Joshi, Nanostructured metal oxide semiconductor-based gas sensors: a comprehensive review, Sens. Actuators A Phys. 341 (March) (2022) 113578, https://doi.org/10.1016/j.sna.2022.113578.

[17] R. Kumar, X. Liu, J. Zhang, M. Kumar, Room-Temperature Gas Sensors Under Photoactivation: From Metal Oxides to 2D Materials, 12, Springer, Singapore, 2020, https://doi.org/10.1007/s40820-020-00503-4.

[18] N. Tao, Challenges and Promises of Metal Oxide Nanosensors, ACS Sens. 4 (4) (2019) 780, https://doi.org/10.1021/acssensors.9b00622.

[19] F. Pang, S. Cheng, H. Yang, W. Hu, Oleylamine-functionalized graphene oxide in wearable flexible organic field-effect transistors for ultrasensitive NH_3 Detection, ACS Sens. 10 (6) (2025) 4318–4328, https://doi.org/10.1021/acssensors.5c00563.

[20] B. Li, et al., A fuel cell type gas sensor based on $Pt/Ti_3C_2T_x$ MXene for highly selective detection of NH3, Mater. Lett. 383 (ember 2024) (2025) 137979, https://doi.org/10.1016/j.matlet.2025.137979.

[21] J.K. Ko, I.H. Park, K. Hong, K.C. Kwon, Recent advances in chemoresistive gas sensors using two-dimensional materials, Nanomaterials 14 (17) (2024), https://doi.org/10.3390/nano14171397.

[22] L. Zhang, K. Khan, J. Zou, H. Zhang, Y. Li, Recent advances in emerging 2D material-based gas sensors: potential in disease diagnosis, Adv. Mater. Interfaces 6 (22) (2019) 1–27, https://doi.org/10.1002/admi.201901329.

[23] X. Tian, et al., Recent advances in MoS_2-based nanomaterial sensors for room-temperature gas detection: A review, Sens. Diagn. 2 (2) (2023) 361–381, https://doi.org/10.1039/d2sd00208f.

[24] S. Mehdi Aghaei, A. Aasi, B. Panchapakesan, Experimental and theoretical advances in mxene-based gas sensors, ACS Omega 6 (4) (2021) 2450–2461, https://doi.org/10.1021/acsomega.0c05766.

[25] R. Gond, P. Shukla, B. Prakash, B. Rawat, Vertically Aligned MoS_2/ZnO heterostructure for highly selective NH_3 sensing at room temperature, ACS Appl. Electron. Mater. 6 (4) (2024) 2728–2738, https://doi.org/10.1021/acsaelm.4c00264.

[26] E. Afsharmanesh, H. Haratizadeh, F. Bagheri, Self-powered, highly selective and fast response time ammonia gas sensors based on an rGO/SnO_2 nanocomposite, Sens. Actuators A Phys. 379 (August) (2024) 115963, https://doi.org/10.1016/j.sna.2024.115963.

[27] T. Thi Nguyet, et al., Transition from p-type to n-type semiconductor in V_2O_5 nanowire-based gas sensors: Synthesis and understanding of the sensing mechanism, Sens. Actuators B Chem. 424 (1) (2025) 136841, https://doi.org/10.1016/j.snb.2024.136841.

[28] R. Alrammouz, et al., V_2O_5 gas sensors: a review, Sens. Actuators B. Chem. 332 (2021) 113179, https://doi.org/10.1016/j.sna.2021.113179.

[29] K. Schneider, M. Lubecka, A. Czapla, V_2O_5 thin films for gas sensor applications, Sens. Actuators B. Chem. 236 (2016) 970–977, https://doi.org/10.1016/j.snb.2016.04.059.

[30] A.A. Akande, T. Mosuang, C.N.M. Ouma, E.M. Benecha, T. Tesfamichael, K. Roro, Ammonia gas sensing characteristics of V_2O_5 nanostructures: a combined experimental and ab initio density functional theory approach, J. Alloy. Compd. 821 (2020) 153565, https://doi.org/10.1016/j.jallcom.2019.153565.

[31] R. Saad, RSC Advances improved optical and CO_2 gas sensing, RSC Adv. (2026) 196–207, https://doi.org/10.1039/d5ra07026k.

[32] A.D. Raj, P.S. Kumar, Q. Yang, D. Mangalaraj, Synthesis and gas sensors behavior of surfactants free V_2O_5 nanostructure by using a simple precipitation method, Phys. E Low. Dimens. Syst. Nanostruct. 44 (7–8) (2012) 1490–1494, https://doi.org/10.1016/j.physe.2012.03.016.

[33] L.A. Burton, A. Walsh, Phase stability of the earth-abundant Tin Sul fi des SnS, SnS_2, and SnS_3, Phys. Chem. C. 116 (45) (2012) 24262–24267, https://doi.org/10.1021/jp309154s.

[34] B. Zhao, et al., High-order superlattices by rolling up van der Waals heterostructures, Nature 591 (7850) (2021) 385–390, https://doi.org/10.1038/s41586-021-03338-0.

[35] C. Guo, et al., Two-dimensional SnS_2 single crystal for sensitive NO_2 detection at room temperature, Micro Nanoeng. 11 (2025) 246, https://doi.org/10.1038/s41378-025-01054-7.

[36] J. Sun, W. Xiong, J. Zhang, Y. Zhang, B. Xie, SnS_2 nanoparticle-based gas sensor with highly sensitive NO_2 detection at room temperature, Mater. Lett. 308 (PB) (2022) 131214, https://doi.org/10.1016/j.matlet.2021.131214.

[37] X. Xu, S. Ma, X. Xu, S. Pei, T. Han, W. Liu, Transformation synthesis of heterostructured SnS_2/ZnS microspheres for ultrafast triethylamine detection, J. Alloy. Compd. 868 (2021) 159286, https://doi.org/10.1016/j.jallcom.2021.159286.

[38] Q. Zhang, S. Ma, R. Zhang, K. Zhu, Y. Tie, S. Pei, Optimization NH_3 sensing performance manifested by gas sensor based on Pr-SnS_2/ZnS hierarchical nano, fl owers 807 (2019) 2–10, https://doi.org/10.1016/j.jallcom.2019.151650.

[39] Z. Lei, et al., Glucose-modulated defect-enriched Sv-SnS_2 sensor for rapid detection of NH_3 at room temperature, J. Alloy. Compd. 1026 (December 2024) (2025) 180379, https://doi.org/10.1016/j.jallcom.2025.180379.

[40] C. Liang, P. Li, S. Yu, Q. Jing, Y. Niu, Design and mechanism study of fast response MoS 2 / SnS 2 heterojunction ammonia sensor for gas detection in chicken coops, J. Alloy. Compd. 1022 (December 2024) (2025) 179906, https://doi.org/10.1016/j.jallcom.2025.179906.

[41] L. Zhang, J. Xu, X. Lei, H. Sun, T. Ai, Applied surface science highly selective ammonia detection by SnS 2 nanosheets functionalized Ti 3C 2 T x, Appl. Surf. Sci. 712 (July) (2025) 164190, https://doi.org/10.1016/j.apsusc.2025.164190.

[42] X. Jiang, Y. Zhen, Y. Feng, Z. Yang, Z. Qin, Synthesis of SnS2/SnO2 nano-heterojunctions with increased reactive sites and charge transfer for ultrasensitive NH3 detection, J. Alloy. Compd. 938 (2023) 168520, https://doi.org/10.1016/j.jallcom.2022.168520.

[43] T.T. Nguyet, C.M. Hung, H.S. Hong, N.X. Thai, et al., Enhanced response characteristics of NO_2 gas sensor based on ultrathin SnS_2 nanoplates: experimental and DFT study, Sens. Actuators A Phys. 373 (2024) 115384, https://doi.org/10.1016/j.sna.2024.115384.

[44] A. Cao, J. Hu, H. Liang, L. Wan, Self-assembled vanadium pentoxide (V_2O_5) hollow microspheres from nanorods and their application in lithium-ion batteries, 4391-5, Angew. Chem. Int 44 (28) (2005) 4391–4395, https://doi.org/10.1002/anie.200500946.

[45] X. Jiang, Y. Wang, Y. Xia, Ethylene glycol-mediated synthesis of metal oxide nanowires, J. Mater. Chem. 14 (2004) 695–703, https://doi.org/10.1039/B313938G.

[46] T. Mo, S. Chen, Physical characterization and electrical properties of chelating-agents added PZT films, Ferroelectrics (2011) 305–310, https://doi.org/10.1080/00150190108008752.

[47] A. Siabi-garjan, Photonics and nanostructures - fundamentals and applications A comprehensive study on the Rod-based plasmonic structures sensing using the modified discrete dipole approximation method, Photonics Nanostruct. Fundam. Appl. 58 (December 2023) (2024) 101224, https://doi.org/10.1016/j.photonics.2023.101224.

[48] P. Rai, W. Kwak, Y. Yu, Solvothermal Synthesis of ZnO nanostructures and their morphology-dependent gas-sensing properties, 24, ACS Appl. Mater. Interfaces 5 (8) (2013) 3026–3032, https://doi.org/10.1021/am302811h.

[49] J. Ma, D. Lei, L. Mei, et al., Plate-like SnS_2 nanostructures: hydrothermal preparation, growth mechanism and excellent electrochemical properties, Cryst. Eng. Comm. 14 (2012) 832–836, https://doi.org/10.1039/c1ce05831b.

[50] T.T. Nguyet, et al., Enhanced response characteristics of NO_2 gas sensor based on ultrathin SnS_2 nanoplates: Experimental and DFT study, Sens. Actuators A Phys. 373 (2) (2024) 1–14, https://doi.org/10.1016/j.sna.2024.115384.

[51] H. Zhong, et al., Vertically Aligned Graphene-Like SnS_2 ultrathin nanosheet arrays: excellent energy storage, catalysis, photoconduction, and field- emitting performances, J. Phys. Chem. C. 116 (16) (2012) 9319–9326, https://doi.org/10.1021/jp301024d.

[52] H. Song, C. Zhang, Y. Liu, C. Liu, X. Nan, G. Cao, Facile synthesis of mesoporous V_2O_5 nanosheets with superior rate capability and excellent cycling stability for lithium ion batteries, J. Power Sources 294 (2015) 1–7, https://doi.org/10.1016/j.jpowsour.2015.06.055.

[53] S. Tang, J. Yu, Interfacial interaction of Ag nanoparticles with graphene oxide supports for improving NH_3 and NO adsorption: a first-principles study, Phys. Chem. Chem. Phys. 18 (2016) 7797–7807, https://doi.org/10.1039/c5cp07399e.

[54] H. Du, et al., A new model and its application for the dynamic response of rgo resistive gas sensor, Sens. (Switz.) 19 (4) (2019) 1–11, https://doi.org/10.3390/s19040889.

[55] A.G. Bannov, M.V. Popov, A.E. Brester, P.B. Kurmashov, Recent advances in ammonia gas sensors based on carbon nanomaterials, Micromachines 12 (2) (2021), https://doi.org/10.3390/mi12020186.

[56] X. Zhou, K. Niu, Z. Wang, L. Huang, L. Chi, An ammonia detecting mechanism for organic transistors as revealed by their recovery processes, Nanoscale 10 (18) (2018) 8832–8839, https://doi.org/10.1039/c8nr01275j.

[57] Á. Peña, et al., Optimization of multilayer graphene-based gas sensors by ultraviolet photoactivation, Appl. Surf. Sci. 610 (October 2022) (2023), https://doi.org/10.1016/j.apsusc.2022.155393.

[58] D. Kim, G. Cha, J. Woo, J. Noh, J. Park, UV-assisted ammonia sensing at room temperature Using Ga_2O_3/Ti_3C_2Tx mxene composite, 2025 23rd Int. Conf. SolidState Sens. Actuators Microsyst. 2 (July) (2025) 1101–1104, https://doi.org/10.1109/Transducers61432.2025.11109721.
[59] A. Beniwal, Sunny, UV Treated sol-gel synthesized SnO_2-polypyrrole sensor for ultra-low ammonia detection at RT, Proc. IEEE Sens. 2019-Octob (2019) 1–4, https://doi.org/10.1109/SENSORS43011.2019.8956656.
[60] K. Lin, et al., A V_2O_5/MWCNTs composite thin film gas sensor for the fast detection of ammonia, Mater. Today Commun. 38 (ember 2023) (2024), https://doi.org/10.1016/j.mtcomm.2023.107969.
[61] L. Van Duy, et al., Light-assisted room temperature ammonia gas sensor based on porphyrin-coated V_2O_5 nanosheets, Sens. Actuators B Chem. 409 (February) (2024) 135582, https://doi.org/10.1016/j.snb.2024.135582.
[62] I. Raible, M. Burghard, U. Schlecht, A. Yasuda, T. Vossmeyer, V_2O_5 nanofibres: novel gas sensors with extremely high sensitivity and selectivity to amines, Sens. Actuators B Chem. 106 (2005) 730–735, https://doi.org/10.1016/j.snb.2004.09.024.
[63] H. Khan, K. Malook, M. Shah, Highly selective and sensitive ammonia sensor using polypyrrole/V_2O_5 composites, J. Mater. Sci. Mater. Electron 28 (18) (2017) 13873–13879, https://doi.org/10.1007/s10854-017-7235-5.
[64] Y.L. Pan, W.C. Liu, Study of a platinum (Pt) nanoparticle (NP)/Vanadium pentoxide (V_2O_5) thin film-based ammonia gas sensor, IEEE Trans. Electron Devices 67 (5) (2020) 2126–2132, https://doi.org/10.1109/TED.2020.2981113.
[65] S.N. Birajdar, N.Y. Hebalkar, S.K. Pardeshi, Ruthenium-decorated vanadium pentoxide for, RSC Adv. 9 (2019) 28735–28745, https://doi.org/10.1039/c9ra04382a.
[66] C. Wang, et al., Sensors and Actuators B: Chemical Effects of sintering temperature on sensing properties of V_2O_5 -WO_3 -TiO_2 electrode for potentiometric ammonia sensor, Sens. Actuators B. Chem. 241 (2017) 268–275, https://doi.org/10.1016/j.snb.2016.09.117.
[67] H. Fu, X. Yang, X. An, W. Fan, X. Jiang, A. Yu, Sensors and Actuators B: Chemical Experimental and theoretical studies of V_2O_5 @TiO_2 core-shell hybrid composites with high gas sensing performance towards ammonia, Sens. Actuators B. Chem. 252 (2017) 103–115, https://doi.org/10.1016/j.snb.2017.05.027.
[68] J. Wang, H. Shen, Y. Xia, S. Komarneni, Light-activated room-temperature gas sensors based on metal oxide nanostructures: a review on recent advances, Ceram. Int. 47 (6) (2021) 7353–7368, https://doi.org/10.1016/j.ceramint.2020.11.187.
[69] M. Adhikari, D. Chattopadhyay, D. Saha, M. Pal, Room-temp trace ammonia detection using SnS_2 nanosheets@ PANI composite: a step towards ultrasensitive environment monitoring and non-invasive renal disease diagnosis, Mater. Chem. B 13 (2025) 12480–12492, https://doi.org/10.1039/D5TB01445J.
[70] M. Li, W. Li, High-sensitivity room-temperature NH_3 detection of SnO_2/SnS_2 nanocomposites by modulating annealing temperature, Vacuum 239 (May) (2025) 114401, https://doi.org/10.1016/j.vacuum.2025.114401.
[71] H. Huu, N. Viet, L. Thi, P. Thi, V. Bac, D. Van An, Sensors and actuators: A. Physical Highly sensitive and dual-selective gas sensing using WS_2 nanosheets for NO_2 and NH 3 detection at low temperature, Sens. Actuators A. Phys. 399 (December 2025) (2026) 117464, https://doi.org/10.1016/j.sna.2026.117464.
[72] S. Cai, et al., High-performance ammonia sensor at room temperature based on 2D conductive MOF Cu3(HITP)2, Talanta 285 (2025) 127226, https://doi.org/10.1016/j.talanta.2024.127226.
[73] J. Bai, Y. Shen, S. Zhao, et al., DFT and DRIFTs insights into defect-driven d-band center modulation for selective NH3 sensing in MoS_2-MoO_x heterojunctions, Appl. Surf. Sci. (2025) 165397, https://doi.org/10.1016/j.apsusc.2025.165397.
[74] Y. Qin, Y. Zou, Z. Wang, Applied Surface Science Phase-dependent behavior of VO_2 -based gas sensor and their NH_3 -sensing enhancement via CQDs modification, Appl. Surf. Sci. 723 (August 2025) (2026) 165690, https://doi.org/10.1016/j.apsusc.2025.165690.
[75] H. Yao, Y. Chen, Y. Wei, Z. Zhao, Z. Liu, C. Xu, Surface Science A periodic DFT study of ammonia adsorption on the V_2O_5 (001), V_2O_5 (010) and V_2O_5 (100) surfaces: Lewis versus Brönsted acid sites ☆, Surf. Sci. 606 (21–22) (2012) 1739–1748, https://doi.org/10.1016/j.susc.2012.07.020.
[76] B. Xing, M. Zhang, Z. Zhang, X. Yao, In-doped SnS_2 induced S-vacancies for ammonia-sensitive sensors, Ceram. Int. 51 (18PA) (2025) 25114–25124, https://doi.org/10.1016/j.ceramint.2025.03.193.